STRESS RUPTURE AND FATIGUE IN THIN WALL SINGLE CRYSTAL SUPERALLOYS WITH COOLING HOLES

Eugene Sun, Tab Heffernan and Randy Helmink
Rolls-Royce Corp., 2001 South Tibbs Avenue, Indianapolis, IN 46241, USA

Abstract

High pressure turbine airfoils made of single crystal superalloys are often in the form of thin walls containing numerous small holes. These features, essential for the effective cooling of turbine airfoils, present special stress rupture and fatigue failure mechanisms that are not present in bulk single crystals. The objective of this paper is to further the understanding of stress rupture and fatigue of thin wall structures and to find how mechanical property models ordinarily appropriate for bulk superalloys may be modified for use on thin wall structures. Stress rupture properties of thin wall CMSX-4 single crystals, bare and with three types of coatings, were tested and compared with the stress rupture behavior of bulk materials. A model that captures the degradation mechanisms in thin wall structures and allows a quantitative prediction of the stress rupture time of thin-wall turbine airfoils is introduced. The paper also addresses low cycle fatigue crack initiation at cooling holes by testing thin-wall CMSX-4 single crystals at cyclic load conditions that mimic those found in actual turbine airfoils. Finite element calculations show that, even though the cooling holes are under an overall in-plane compressive stress, local stresses driving fatigue crack development are tensile due to local plastic deformation. With the mechanism-based approach, this work shows that it is possible to modify mechanical behavior models developed for bulk single crystal superalloys so that they can be used for component life calculations of thin wall structures.

Introduction

High pressure turbine airfoils made of single crystal superalloys are often in the form of thin walls containing a large number of small cooling holes. Figure 1 shows examples of such turbine airfoils. Figure 1(a) shows the cross-section of an example thin wall turbine blade where the wall thickness of the thinnest part of the blade is typically of the order of 0.5 mm. Figure 1(b) is a schematic picture of a turbine vane having a multi-wall structure with a spar and thin wall coversheets containing an array of cooling holes.

The thin walls and the small holes are needed for the effective cooling of the airfoils. The wall is made thin so that heat in the external surface of the airfoil can be efficiently transferred, via conduction, to the cooling air that flows in the core passages of the hollow airfoils. The array of small holes form a film of relatively cool air on the external surface of the airfoil that separates the airfoil from the hot gas that flows by.

It has been known for some time that, under the same stress and temperature conditions, stress rupture of superalloys in the form of thin walls happens more rapidly versus thick solid bars. Duhl [1] reported that the thin wall effect was most pronounced in equiaxed superalloy castings, followed by directionally solidified castings, and is smallest in single crystals. Doner and Heckler [2], working on thin wall superalloy samples in the form of tubes and flat plates with and without coatings and tested in air and in a protective atmosphere, concluded that the stress rupture debit was due to environmental degradation of the single crystals, leading to a reduction in the load carrying cross-section, and to grain boundary damage for equiaxed materials. Seetharaman and Cetel [3] systematically tested uncoated PWA1484 single crystals of different wall thicknesses and found that, under a given nominal stress, the initial creep (e.g. creep to 1% strain) is minimally affected by the wall thickness, but that there is significant debit in the stress rupture in thinner sections.
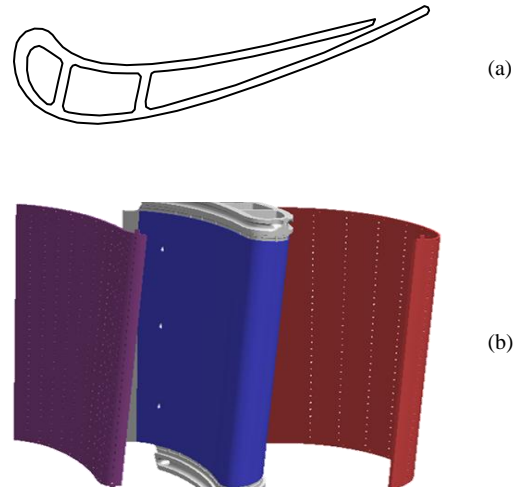

Figure 1. (a) Schematic cross-section of a typical thin-wall hollow turbine blade. (b) Schematic illustration of a multi-wall turbine vane having a spar and thin wall coversheets with arrays of cooling holes.

It is clear, from these previous works, that stress rupture laws developed for superalloys in the bulk form cannot be applied directly to thin wall structures without modification. One objective of this work is to present new test results on coated and uncoated CMSX-4 single crystal thin coupons, and to introduce a new model, by modification of the rupture law of bulk materials, that quantitatively accounts for the thin wall debit and is convenient for rupture life calculations of thin wall airfoils.

Another objective of this work is to address the effect of cooling holes on low-cycle fatigue crack development in thin-wall CMSX-4. Fatigue cracks develop at the cooling holes because the holes are not just sites of stress concentration but also where the material may be damaged locally by the hole drilling process [4, 5]. One further complication typical of thin walls in turbine

airfoils, especially those on the outer surface of multi-wall airfoils such as the coversheet in Figure 1(b), is that the cyclic load on the thin wall is often in the form of in-plane compressive stresses.

This work will present fatigue test results of thin wall CMSX-4 samples with cooling holes prepared using two hole drilling methods that cause different levels of damage to the base material. We will show, through fully plastic finite element calculations, that local tensile stresses are developed at the cooling holes even though the thin walls are under an overall compressive load. We will show that the net impact of the hole drilling process to the fatigue behavior can be evaluated using fatigue laws that are ordinarily appropriate for bulk single crystals

Experimental Details

Thin wall CMSX-4 single crystals loaded in the <001> orientation are studied in this work. Two types of tests were conducted. One is a stress rupture test of 0.51mm thick flat coupons. The other is fatigue test of 0.71 mm thick flat coupons each containing a single 0.51 mm diameter cooling hole.

The sample drawing for stress rupture tests is given in Figure 2. The samples were cast into 0.51mm thick flat coupons, compacted by hot hydrostatic isotropic pressing (HIP) and heat treated per CMSX-4 material specification. The flat faces of the coupons are parallel to a {100} plane. The tensile load direction, shown in Figure 2, is within 10 degrees of <001>. The samples consist of four groups. Three groups were coated and one was uncoated. The three coatings are NiCoCrAlY by electron-beam physical vapor deposition, Pt aluminide by electrophoresis deposition (AEP PtAl), and Pt aluminide by chemical vapor deposition (CVD PtAl). Nominal coating thickness was 50 μm. Inter-diffusion zone thickness was approximately 5 μm for the NiCoCrAlY coating and approximately 30 μm for the Pt aluminide coatings. After coating, the samples were aging heat treated at 870 °C for 20 hours. Stress rupture tests were conducted in air in a resistance-heated furnace at 982 °C, 1038 °C, 1093 °C and 1149 °C using a constant load test machine.
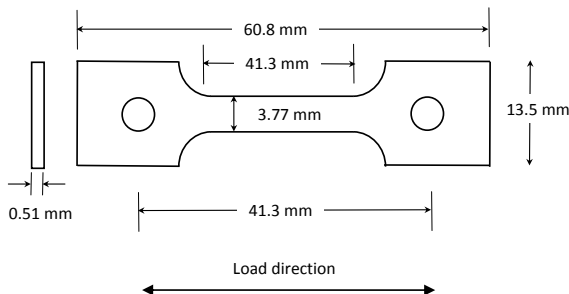

Figure 2. Drawing of thin-wall CMSX-4 single crystal samples for stress rupture tests.

For fatigue tests of thin-wall CMSX-4 with cooling holes, the sample drawing is given in Figure 3. Each sample contains one cooling hole in its center. Hole diameter is 0.51mm. Hole axis is normal to the load direction and is inclined at 30° to the coupon surface, as illustrated in Figure 3. The sample consists of a flat coupon, 2.03 mm in thickness, and a recessed "window" in the center of the coupon, as depicted in Figure 3, where the wall

thickness is 0.71 mm and where the 30° hole is located. The use of the recessed "window" is to prevent buckling as the samples are loaded in compression to simulate the stresses on thin walls in actual turbine nozzle guide vanes. The load direction, along the long axis of the samples, is within 10° of <001>. The flat face of the coupons is parallel to {100}.

The single crystal samples for fatigue testing were made by casting. They were then hot hydrostatically pressed, solution heat treated, coated with CVD Pt aluminide, and given heat treatments that simulated the processing of a typical single crystal turbine airfoil. Figure 4 shows a photographic image of a coated sample and the close-up view of the 30° hole drilled using a mechanical method. Holes created by two different methods, a mechanical method and a waterjet method, were evaluated.

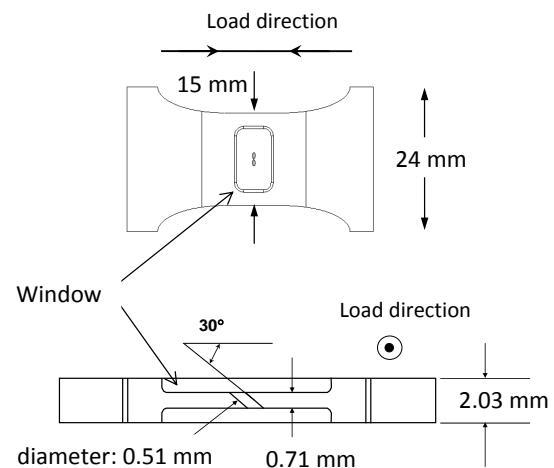Figure 3. LCF sample drawing of thin-wall CMSX-4 with a 30° inclined 0.51 mm diameter hole. The upper part of the figure shows the face of the sample. The lower part of the figure shows sample cross-section viewed along the load direction.
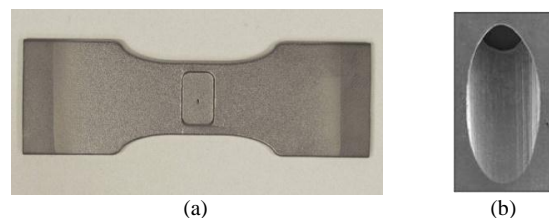

Figure 4. Photographs of a coated CMSX-4 single crystal flat coupon with a 30° hole (a) and a close-up image of a hole prior to coating (b).

Fatigue tests were conducted in air at 927 °C on a test machine with hydraulic actuators. Heating was by induction. Strain was measured using a pair of extension rods positioned over a gage length of 9.5 mm on each side of the recessed window, as shown in Figure 5(a). Testing was strain controlled at 0.33 Hz. The specimens were cycled between 0.27% compressive strain and zero strain to simulate the cyclic strains at the hot flow path of a typical cooled turbine airfoil. The progression of fatigue cracks

was monitored at temperature using a microscopic lens with a long working distance and a crack detection limit of approximately 0.05 mm. Figure 5(b) shows a typical crack that initiated at the corner where the hole intersects the sample surface.

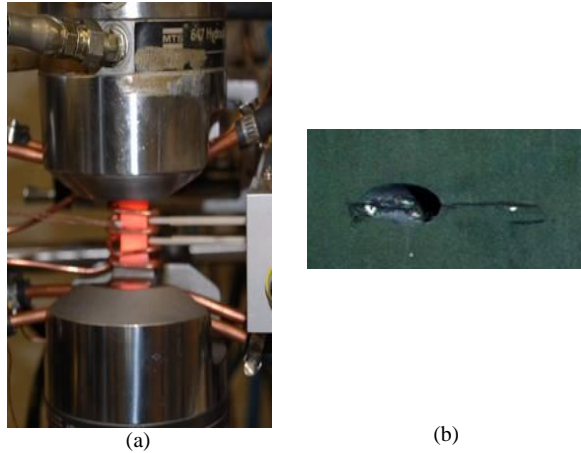(a)   (b)

Figure 5. A photograph of the fatigue test machine showing the induction heating of the sample and the pair of extension rods for measuring and controlling the displacement (a). Cracks are detected optically using a long work distance microscope. An example image of a crack in the acute corner of the hole (b).

Results and Discussions

1. Stress Rupture

The objective of the stress rupture tests and analyses in this work is to find how stress rupture laws developed for bulk superalloys may be modified for use on thin wall structures.

1.1. Test Results

Stress rupture test results of thin-wall CMSX-4 samples with and without coatings are given in Table 1. Here the nominal stress is load divided by the initial cross-sectional area of the samples prior to the application of coatings.

Stress rupture properties of thin-wall samples are compared with solid bars of CMSX-4 (6.35 mm in diameter) in Figure 6 by plotting the nominal stress versus the Larson-Miller parameter (LMP). The solid bars, because of their large diameter, are viewed as unaffected by environmental degradation. The thin wall data points fall significantly below the solid bar curve, as shown in Figure 6, indicating that there is significant degradation to the thin wall samples.

It is well known that environmental coatings, especially diffusion coatings such as Pt aluminide coatings, can degrade the mechanical properties of the surface layer of single crystal superalloys by converting the base material surface microstructure into a microstructure with inferior stress rupture resistance and that the resultant effect on mechanical properties may be corrected by subtracting the diffusion thickness from the sample cross-section in stress calculations [2, 3, 6]. The meaning of the diffusion layer thickness (d_{diff}) is illustrated using a scanning

electron microscope (SEM) image in Figure 7. In the following we will use the term corrected stress σ_{corr} which is load divided by the sample cross-section area that excludes d_{diff}.

Table 1. Stress rupture data for the four types of thin wall samples of CMSX-4. NT stands for "not tested."

| Temp (°C)	Nominal Stress (MPa)	Stress Rupture Time (hours)			
		Bare	NiCoCrAlY	CVD PtAl	AEP PtAl
982	172.4	NT	NT	369.9	269.2
982	206.9	460.1	443.7	162	127.4
982	220.6	331.5	288	135.5	119.5
982	241.3	206.7	214.2	84.5	75.6
982	262.0	162.7	NT	NT	NT
982	275.8	44.7	88.2	34.6	42.7
982	344.8	41.1	32.8	15.5	10.7
1038	110.3	NT	NT	465.1	432.8
1038	124.1	NT	NT	239.4	284.7
1038	137.9	586.2	422.1	197.7	146.2
1038	151.7	266.9	360	64.1	117.8
1038	172.4	163.3	199.5	49	62.5
1038	193.1	71.9	41.2	NT	NT
1038	220.6	42.6	51.8	22.1	18.8
1093	72.4	2445.5	2315.3	711.2	566.7
1093	82.7	2566.2	1437.5	618.7	377.7
1093	96.5	NT	NT	262.9	274.2
1093	103.4	976.9	653.5	111.2	158.9
1093	124.1	275.3	251.9	58.6	64.5
1093	137.9	95.5	116.8	17.3	29.2
1093	151.7	62.8	47.3	NT	NT
1149	31.0	NT	NT	604.7	333.5
1149	41.4	NT	NT	687.2	280.7
1149	55.2	599.4	1045.4	398	128.2
1149	55.2	NT	1179.6	NT	NT
1149	72.4	512.5	286.1	220.8	140.5
1149	75.8	192.7	195.2	210.4	73.4
1149	96.5	109.1	NT	44.8	47.6
1149	103.4	32.9	107	NT	NT
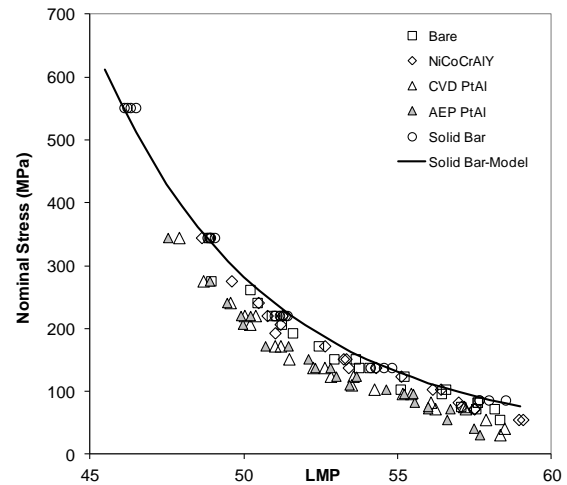
Figure 6. Nominal stress plotted against Larson-Miller parameter for the four types of thin wall samples and solid bars of CMSX-4.

Figure 8 shows the Larson-Miller plots re-plotted in terms of the corrected stress σ_{corr} for the four types of thin wall samples. The thin wall samples still show significant debit relative to the solid

bars of CMSX-4. This shows that correction for the coating diffusion zone alone does not account for all of the degradation to the base material and suggests that there is further degradation to the thin wall samples during their exposure to the high temperatures. This observation is consistent with prior suggestions [1-3] that single crystal superalloys suffer from continuing environmental degradations during service.
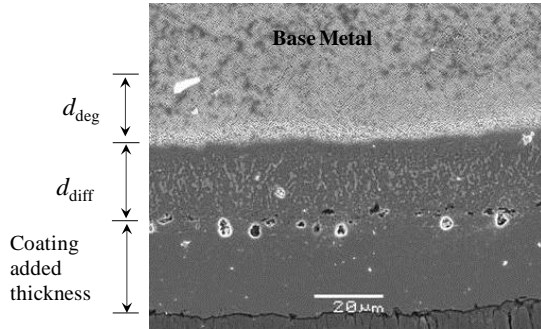

Figure 7. A scanning electron microscope image of a CMSX-4 single crystal coated with Pt aluminide to illustrate the meaning of diffused zone thickness d_{diff} and the degradation thickness d_{deg}.
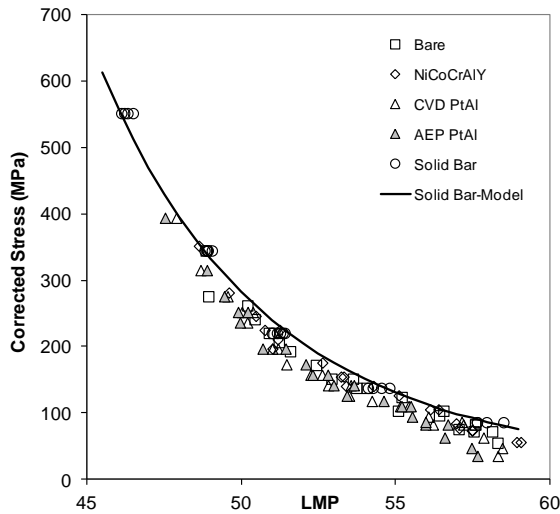

Figure 8. Corrected stress plotted against the Larson-Miller parameter for the four types of thin wall samples and solid bars. The debit in the thin wall samples relative to the solid bars suggests that there is further degradation during the rupture tests.

The environmental degradations may be in the form of oxidation and/or continuing interdiffusion of the base material with the coating material. Both mechanisms produce an outward diffusion of aluminum to form and reform the protective alumina scale during exposure and a resultant loss of gamma prime precipitates in the underlying region. The effects of time and temperature on oxidation and interdiffusion kinetics are well understood, exhibiting power law and Arrhenius behavior respectively [7, 8]. The effects of stress and strain on these phenomena are less well known, but recent work has shown that their effects should not be neglected [9-12]. We will not attempt to separate and quantify

these different degradation mechanisms to the CMSX-4 thin wall single crystals. Our objective here is to find a practical model that accounts for the combined effects of these different degradation processes on stress rupture and has a form simple enough so that it can be readily used for turbine engine component rupture life calculations and its coefficients can be reliably determined from test results.

1.2. Effective Degradation Thickness and Effective Stress

On recognizing that subtracting the inter-diffusion thickness d_{diff} from the sample cross-section does not account for all of the degradation to the thin wall structure, as shown in Figure 8, the next logical step is to subtract the degradation thickness d_{deg} from the sample cross-section and recalculate the actual stress that drives creep and rupture. The degradation thickness (d_{deg}) due to continuing degradation during testing is illustrated in Figure 7. We recognize a number of difficulties in accounting for d_{deg} rigorously, and will therefore make a number of simplifications.

The degraded material in the subsurface region, due to oxidation and the base metal reaction with the coating material, is not expected to lose all of its load carrying capabilities. Its strength against creep and rupture will likely vary with the distance from the surface or the coating. The gradient in the load carrying capacity cannot be easily determined from microscopy or microstructure observations. In this work, we will assume, as a simplification, that the effect of material degradation on stress rupture can be represented by a single thickness d_{deg}, called effective degradation thickness, over which the material has lost all of its strength against rupture. Instead of defining d_{deg} in terms of microstructure and measuring it using microscopy, our approach is to determine d_{deg} directly from stress rupture test data of thin wall samples.

The degradation region is also expected to become thicker with time and hence the instantaneous stress driving creep and rupture would also evolve with time. For this reason, any rigorous analytical solution for the rupture time of thin wall structures would be convoluted, since the constitutive law for rupture time depends on stress which in turn varies with time due to the continuing material degradation in the subsurface region. Such form of solution, though rigorous, would be impractical, not only from the point of view of turbine engine component life calculations, but also from the point of view of determining, through regression, model coefficients from test data. We further recognize that the current constitutive creep and stress rupture laws, such as the Larson-Miller relationship used in this work or the more advanced formalisms (e.g. [13-15]), are still approximate in their predictions. The approximate nature of these laws, in our view, does not justify the use of elaborate formulations to account for the degradation thickness. So, as another simplification, we will assume that the effective degradation thickness d_{deg} is a constant at a given temperature and stress. In essence, we assume that the continuing degradation during the time up to stress rupture can be represented by a single, effective degradation thickness d_{deg}, and that the sample is therefore under an effective stress σ_{eff}, unchanging with time, which is found by subtracting d_{deg} from the load carrying cross-section.

The analyses below show that the effective degradation thickness concept allows the development of a practical model for

356

calculating the stress rupture life of thin wall superalloys and that the model's predictions are in good agreement with test data.

Since the degradation thickness is derived from the stress rupture data, specifying two of the parameters in time, temperature, and stress space uniquely determines the third parameter. While it may be more natural to relate these diffusion controlled mechanisms of d_{deg} growth to time, the structural analysts supporting turbine airfoil designs require degradation to be expressed relative to stress. In the design process, time is specified from the engine service requirements and temperature is controlled by the gas path and cooling air temperatures, the cooling methodology, and the cooling air allotment. In other words, the notion of the effective degradation thickness as function of temperature and stress is also convenient to turbine engine stress and life analysts.

The effective degradation thickness d_{deg}, as defined above, would obviously decrease with increasing stress at a given temperature, since a higher stress leads to a shorter rupture time which in turn means a smaller degradation thickness. For example, the effective degradation thickness under a very high stress should be very close to zero because rupture under high stresses may take place well before any significant degradation has time to develop.

How the effective degradation thickness changes with temperature is difficult to predict from first principles. At a given stress, increasing the temperature increases the rate at which the material is degraded, but it also causes the total degradation time to decrease due to the shortened rupture time. Namely, the effective degradation thickness may increase or decrease with temperature depending on whether the degradation rate or the rupture time is more sensitive to changes in temperature. In this work, the net effect of temperature on the effective degradation thickness was determined from regression analysis of stress rupture test data. Namely the resultant model represents the effects of temperature on degradation rate and rupture time combined.

From the effective degradation thickness d_{deg} we can define the effective stress σ_{eff} which, for a thin wall sample with a rectangular cross section, is given by

$$\sigma_{eff} = \frac{\sigma_{corr}}{\left(1 - 2\frac{d_{deg}}{A}\right)\left(1 - 2\frac{d_{deg}}{B}\right)} \qquad (1)$$

where A and B are the lengths of the two sides of the rectangle after correction for the diffusion thickness, and σ_{corr} is corrected stress also found after correction for the coating diffusion thickness. With A, B and σ_{corr} known, Equation (1) allows the determination of the degradation distance d_{deg} from the effective stress σ_{eff}, and vice versa. Here the rectangular thin wall sample is exposed to environmental damage on all its sides or coated on all of its surfaces in the case of degradation due to reaction with coating material. For thin walls in turbine airfoils, only those surfaces exposed to degradation environments would need correction.

In the following, we will first measure the effective stress from stress rupture test data, and will then find from it the effective degradation thickness using Equation (1). Then multi-variable regression will be used to find how the effective degradation thickness varies with stress and temperature.

The effective stress σ_{eff} can be found from the rupture test data by comparing the Larson Miller data points of thin-wall samples with the Larson-Miller curve for the solid bar, as shown in Figure 9. Whereas the corrected stress σ_{corr} is what drives the creep of the thin-wall sample at the beginning of the rupture test, the actual stress must be higher due to continuing degradation. Since the effective degradation thickness is one over which the degraded material has lost all of its strength against rupture, the effective stress is simply the stress that would cause the solid bar to rupture in the same time or to the same Larson Miller parameter. Thus, as shown graphically in Figure 9, the effective stress can be found as the intersection between the solid bar Larson-Miller curve and a vertical line through the thin wall test data point. The above allows, for each thin wall sample stress rupture test, the measurement of the effective stress σ_{eff} and then from it the effective degradation thickness d_{deg} using Equation (1).
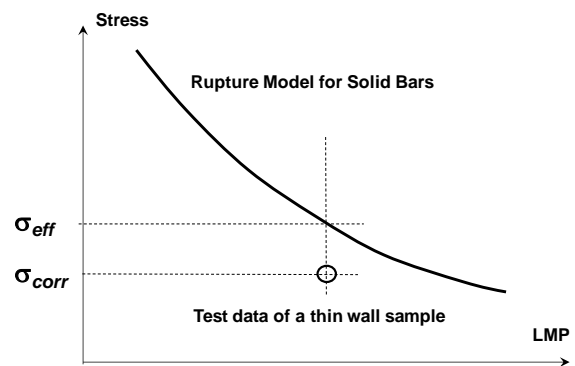

Figure 9. Graphical illustration of the method for finding the effective stress σ_{eff} from the rupture test data of a thin wall sample and the Larson-Miller model of solid bars.

1.3. Dependence of Effective Degradation Thickness on Stress and Temperature

The effective degradation thickness d_{deg} measured from the test data using the method explained above is found to vary with stress and temperature following a power-law Arrhenius-type relationship expressed by Equation (2) below,

$$d_{deg} = d_0 \cdot \sigma_{corr}^n \cdot exp\left(\frac{Q}{RT}\right) \qquad (2)$$

where d_0, n and Q are model coefficients that are determined by regression of test data. Figure 10 below shows, for thin wall samples with AEP Pt aluminide coatings, test data together with the regression plots for the four temperatures tested. The approximate linear relationship in Figure 10 between the logarithm of the degradation thickness and the logarithm of corrected stress demonstrates the power-law relationship of Equation (2). The slope of the regression plots of Figure 10 gives the stress exponent n.

The exponential relationship between the effective degradation thickness and temperature is shown in Figure 11 by plotting the logarithm of the stress-independent term of the degradation thickness against the inverse of temperature. The slope of the regression plot of Figure 11 gives the activation energy Q/R.

The model coefficients d_0, n and Q determined from regression of test data are given in Table 2 for bare and coated thin wall samples. It is noted that n is negative and that Q is positive, meaning that the effective degradation thickness d_{deg} decreases with increasing stress or increasing temperature. This is true for both bare thin wall samples where the degradation is due to oxidation and coated samples where the degradation is due principally to base material reaction with the coatings.
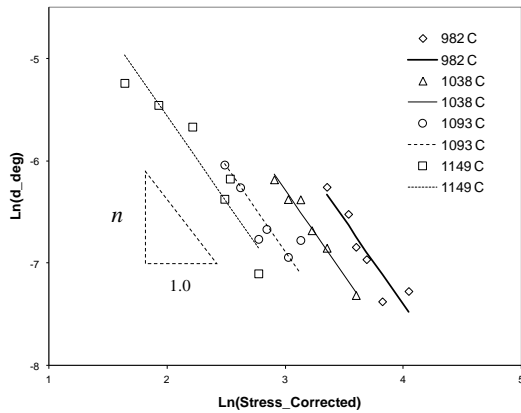

Figure 10. Power-law relationship between the effective degradation thickness (in inch) and the corrected-stress (in ksi) for thin-wall samples with AEP Pt aluminide coating. The symbols represent test data points. The straight lines represent the regression results.
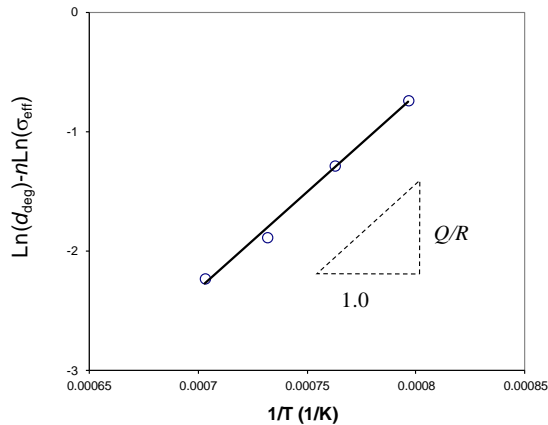

Figure 11. Exponential dependence of the degradation thickness on temperature shown by plotting the logarithm of the stress-independent component of $Ln(d_{deg})$ against the inverse of temperature. Thin wall CMSX-4 coated with AEP Pt aluminide.

The decrease of the effective degradation thickness with stress is expected since, as noted before, at a given temperature a higher stress results to a shorter rupture time and hence less degradation to the material over the course of rupture tests. This shows that the applied stress has a much greater effect on the rupture life than on the degradation reaction rate.

The decrease of effective degradation thickness with temperature shows that rupture time is more sensitive to temperature change than the degradation reaction rate. With any increase in temperature, the degradation reaction rate increases, but the shortening in the rupture time more than compensates the rate increase, leading to an effective degradation thickness that decreases with temperature. We note that the activation energy Q determined through regression of test data represents the effects of temperature on rupture and degradation reaction combined.

Table 2. Coefficients for the effective degradation thickness model determined by regression of test data.

	Bare	NiCoCrAlY	CVD PtAl	AEP PtAl
d_0 (mm)	8.67×10^{-5}	3.18×10^{-6}	2.01×10^{-3}	4.46×10^{-4}
n	-2.062	-3.011	-1.539	-1.667
Q (J/mol)	176000	261000	115000	136000

Figure 12 shows Larson-Miller plots of all four types of thin wall samples re-plotted in terms of the effective stress found using Equations (1, 2) and the coefficients in Table 2. All of the data points collapse around the model curve for solid bars, confirming that the proposed model adequately represents the stress rupture behavior of thin wall structures.
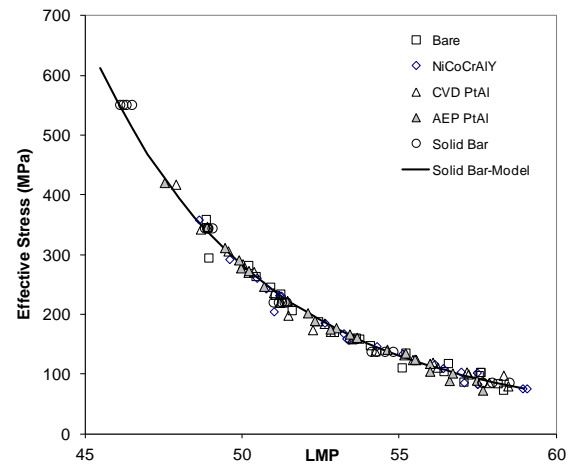

Figure 12. Larson Miller plots for the four types of thin wall samples plotted in terms of the effective stress, together with the stress rupture model of solid bars.

The above model may be applied to the rupture life calculation of turbine airfoils through the following steps. First, the corrected stress σ_{corr} is found by subtracting the coating diffusion thickness from the nominal load carrying cross-section of the component. No correction is needed for areas of the part that are not coated. Second, the effective degradation thickness is found using Equation (2) and the model coefficients which, for CMSX-4, are determined from test data and given in Table 2. Third, the effective stress is found by further subtracting the effective degradation thickness from component cross-section. For parts with a rectangular cross-section under a uniform stress and all faces exposed to the degradation environment, the effective stress is given by Equation (1). For actual parts, only those surfaces that are exposed to a degradation environment, i.e. a high temperature and air or coating material, need correction for the effective degradation thickness. Finally, the effective stress and

temperature are used to find rupture time using stress rupture laws developed from solid bars.

The above approach can be used with any constitutive stress rupture laws. The rupture law for solid bars used in this work is the Larson-Miller relationship. Other stress rupture laws may be used too.

2. Fatigue Cracking at Cooling Holes

Cooling holes affect the fatigue properties of thin wall structures because the holes, like notches, are sites of stress concentration and because the surfaces of the holes may be damaged by the hole drilling process. The effects of notches on fatigue under simple load cycles, especially those with a mean tensile stress, are relatively well understood. External thin wall sections in multi-wall turbine airfoils are typically under an in-plane compressive load. The objective of the fatigue tests and analyses in the following is to demonstrate that fatigue laws developed from and hence ordinarily valid for solid bars can be used to predict fatigue crack development at the cooling holes under compressive in-plane stresses and that the predictions allow the effect of hole drilling process on fatigue to be evaluated.

2.1. Test Results

Thin wall samples of CMSX-4 were tested at 927 °C by cycling the strain at 0.33 Hz between 0 and 0.27% nominal compressive strain. It is noted that, due to the hole and the recessed window in the flat coupon for suppressing buckling, the strain in the sample is not uniformly distributed. The 0.27% strain is a nominal strain defined for a gage length of 9.5 mm over the recessed window and measured using a pair of extension rods as shown in Figure 5.

The cycling strain profile for the fatigue tests is triangular as shown in Figure 13. The temperature and strain cycle profile were selected to mimic the condition found on a typical high pressure turbine nozzle guide vane. The in-plane compressive strain is a result of the external skin of the airfoil undergoing thermal expansion against the relatively cooler core of the hollow airfoils.
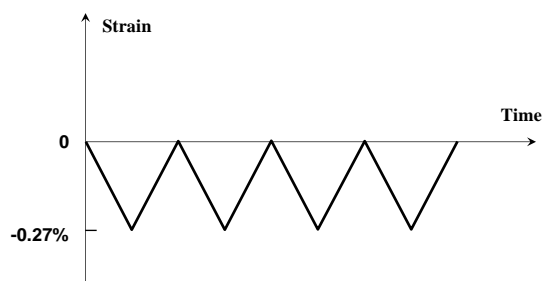

Figure 13. Strain cycle profile used for the fatigue testing of thin wall samples of CMSX-4 with small cooling holes.

Samples containing holes that are same in geometry but prepared by two different methods, a mechanical method (Method A) and waterjet drilling method (Method B), were tested. The samples were from the same batch of castings and given the same Pt aluminide diffusion coating and heat treatments.
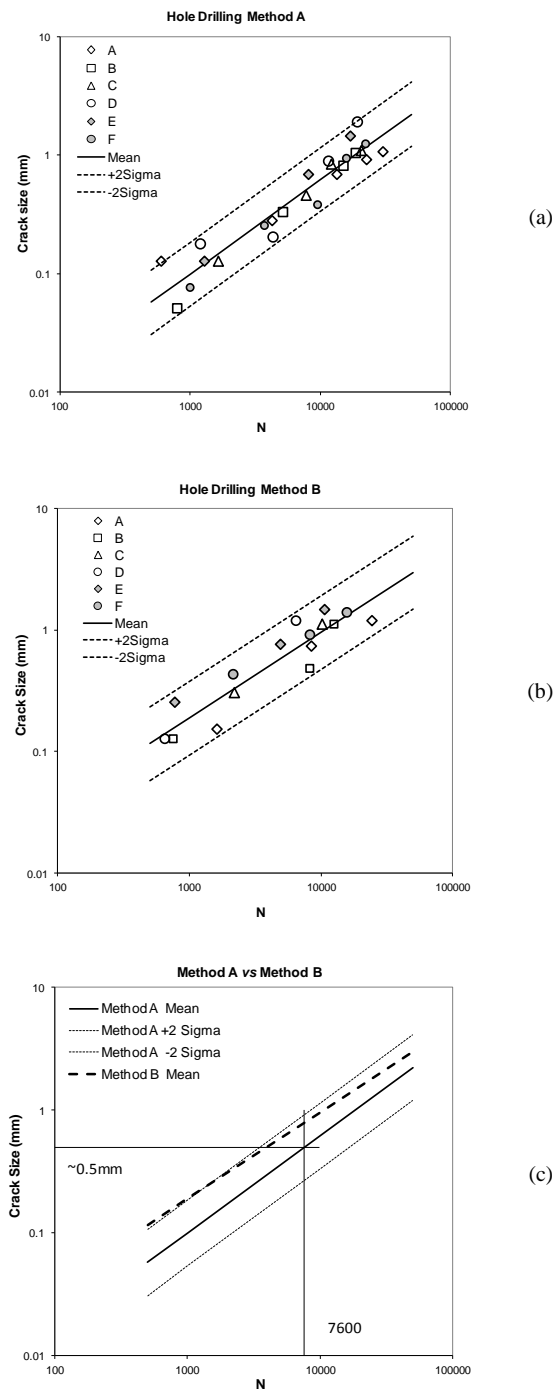

(a)

(b)

(c)

Figure 14. Fatigue crack development with cycle number in six samples with holes drilled with method A (a) and six samples with holes drilled with method B (b), showing the mean behavior and the ±2 Sigma behavior. Methods A and B are compared in (c).

Figure 14(a) shows the test results for samples with holes drilled with Method A by plotting the crack size versus the fatigue cycle number, both on the logarithmic scale. Linear regression between the logarithm of crack size and the logarithm of cycle number gives the mean and the ±2 Sigma curves in Figure 14, where Sigma is the standard deviation. Cracks smaller than the resolution limit of the telescopic lens, 0.05mm, were not included. Figure 14(b) shows the result for samples containing holes drilled using Method B. The two methods are compared in Figure 14(c) by plotting the mean behavior of Method B with the mean and the ±2 Sigma behavior of Method A. Figure 14(c) shows that whereas fatigue crack developments for holes prepared using Methods A and B appear to eventually converge at large cycle numbers (>10,000), the early stages of crack developments for the two methods are different. It takes fewer cycles for fatigue cracks to develop at holes prepared using Method B than Method A.

The reduced fatigue crack development life found in samples with Method B holes may be explained as the result of the greater damage to the surface of the holes in Method B than in Method A. Figure 15 shows scanning electron microscope (SEM) images of Method A and Method B holes, where a damaged region of heavily cold worked material up to 10 microns thick is present on the surface of Method B holes. This damaged region is susceptible to recovery and recrytallization transformations during subsequent treatment and testing. However, as Figure 14 shows and further demonstrated later, hole drilling methods do not appear to cause significant debits to the development of large fatigue cracks.
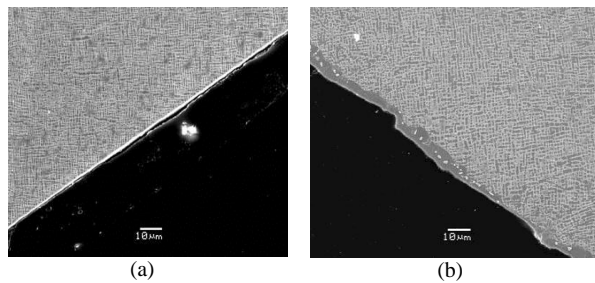

(a)   (b)

Figure 15. SEM images of the surface regions of samples with holes prepared with Method A (a) and Method B (b). The surface region of Method B holes consists of a layer of damaged layer which is much thicker than found on Method A samples. The base metal microstructures appear somewhat different due to the different crystal orientations.

2.2. Fatigue Cracking at the Cooling Holes

In all of the samples tested, cracks were found to initiate at the acute corners where the 30° inclined holes intersect with the thin-wall sample surface. An example is shown in Figure 16(a). Figure 16(b) is a schematic drawing to show the two acute corners where cracks initiate. Cracks were found to start at one corner followed soon by crack initiation at the other similar corner on the other face of the thin wall sample. The test results of Figure 14 represent the cracks that developed first.

Whereas the thin walls are under a compressive in-plane stress, the local stresses at the acute corners of the cooling holes are tensile due to location plastic deformation. The local tensile stresses at the corners of the holes can be seen to develop through

the following steps. At the point when the sample is fully compressed (Figure 17(a)), the thin wall sample is compressed elastically except in the acute corners of the cooling holes where the stress is concentrated sufficiently to cause the local material to deform plastically in compression. As the overall strain is cycled back to zero (Figure 17(d)), the sample restores back to its starting state elastically except the acute corners which, due to its prior plastic deformation in compression, are now under a tensile stress. It is cycling with this local tensile stress that drives the fatigue crack to initiate and propagate under the nominally compressive cycling load.
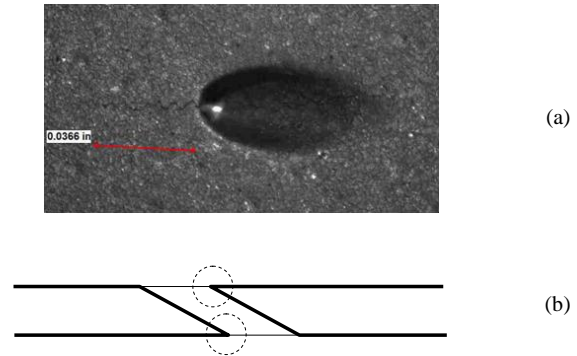

(a)

(b)

Figure 16. An optical microscope image of a fatigue crack at an acute corner of a hole prepared using Method A (a). A schematic illustration of a thin wall with an inclined hole. The two acute corners where fatigue cracks initiate are circled (b).

We used finite element analysis to calculate the stress and strain distribution around the cooling holes at the compressed and relaxed points of the fatigue strain cycle, shown in Figure 17(a) and Figure 17(d) respectively. The cyclic stress-strain curve of CMSX-4 at 927 °C is used for the finite element calculations. In contrast to the usual stress-strain curve measured using tensile tests, cyclic stress strain curves are obtained from fatigue tests of smooth bars of CMSX-4 after a sufficiently large number of cycles, typically at the half of fatigue life, when any strain softening or hardening has exhausted and the hysteresis loops have stabilized. This is also likely the point where the primary creep has been exhausted and the material is undergoing steady state creep that is usually associated with the slowest creep rate.

Figures 17(b) and 17(c) show the stress and strain distribution around the hole when the thin wall sample is under full compression during the strain cycle. As expected, compressive stresses are concentrated at the acute corner of the hole, where the compressive axial stress is maximum at 170.1 ksi (1172.8 MPa) and the maximum total axial strain is 4.09% also in compression. This strain includes elastic and plastic components. The compressive plastic strain at the root of the acute corner (not shown in Figure 17(c)) is 3.04%.

Figures 17(e) and 17(f) show the stress and strain distribution when the sample is returned to zero nominal strain. At the acute corner of the hole, the axial stress is maximum at 147.3 ksi (1015.6 MPa) and tensile (Figure 17(e)). This local tensile stress, as discussed before, is the result of prior local plastic deformation in compression and is what drives the fatigue crack to initiate and grow. The strain at the root of the acute corner is still compressive
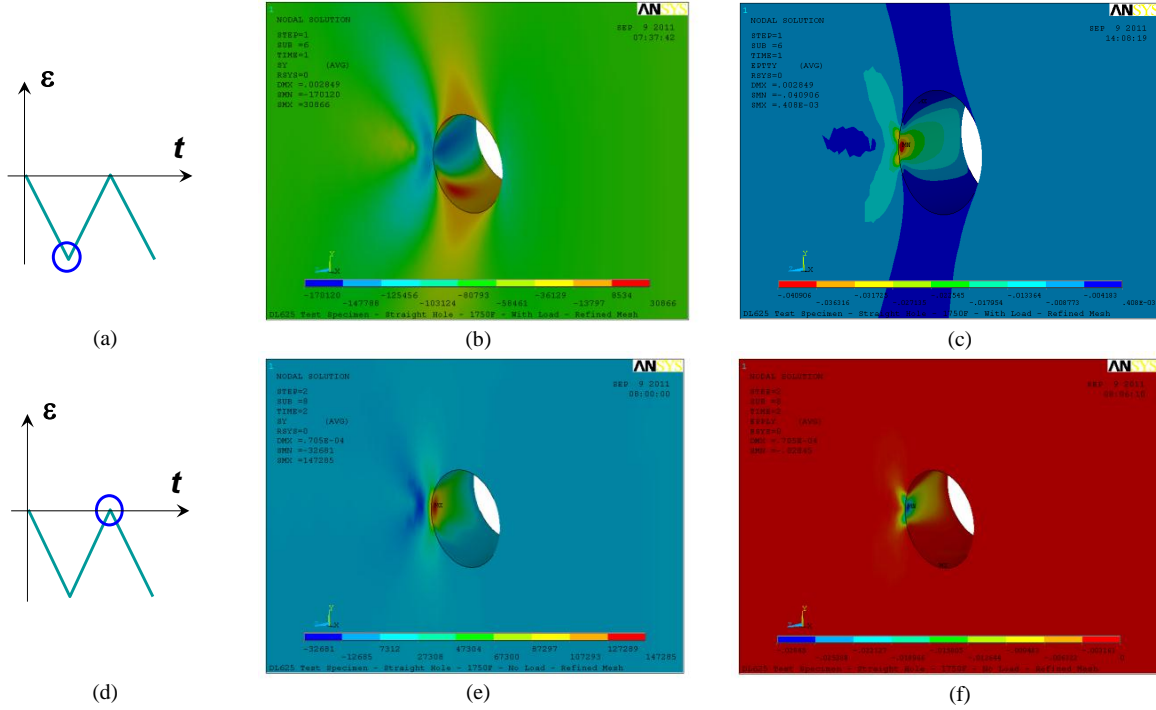
(a)

(b)

(c)

(d)

(e)

(f)

Figure 17. Finite element stress calculations for the 30° holes. The stress (in psi) and strain distributions at the compression point of the strain cycle are shown in (b) and (c) respectively. The stress and strain distributions at the relaxed point of the strain cycle are shown in (e) and (f) respectively.

at 2.8%. It is noted that whereas the local stress at the acute corner of the hole is tensile, the far-field stress is compressive.

The above gives a local (i.e. at the root of the acute corner) strain range of 1.29% with each fatigue cycle and a maximum local tensile stress of 147.3 ksi (1015.6 MPa).

Materials, especially cast materials such as single crystal superalloys, are usually not fully sensitive to notches (as cooling holes are), namely the actual stress driving fatigue crack initiation is not the maximum stress at the notch root but a lower stress. One way to represent the lack of total notch sensitivity is in terms of the fatigue notch sensitivity Q defined below,

$$Q = \frac{K_f - 1}{K_t - 1} \qquad (3)$$

where K_t is the theoretical stress concentration factor and K_f is the fatigue notch factor [16]. Notch sensitivity Q is treated as a material property, allowing the calculation of the fatigue notch factor K_f from Q and K_t, and in turn the calculation of the stress driving fatigue cracking from K_f and a far-field or nominal stress.

In this case, however, the stress concentration factor K_t, defined as the ratio of the local stress to the far-field stress or the nominal applied stress, is not definable because the far-field stress (compressive) is of an opposite sign to the local stress (tensile) in the corners of the holes. Namely, the cooling hole is not a simple stress riser – it also reverses the sign of the local and far-field stresses as a result of local plastic deformation.

In the following, we will make use of the subsurface depth method, also known as the critical distance method, to evaluate the effect of these stresses on fatigue crack development at the cooling holes. In this method, fatigue cracking is treated as initiating at a critical distance below the notch-root where the stress has attenuated from its peak at the root of the notch [17, 18]. The critical distance is found by regressing fatigue test data from smooth bars and notched bars of various known stress concentration factors. For CMSX-4 at 927 °C, the critical distance is 0.05 mm (unpublished internal Rolls Royce data). At 0.05 mm from the root of the acute corners of the hole, finite element analysis gives a tensile stress of 56.1 ksi (387 MPa) and a strain range of 1.05%. Applying the above strain range and max stress to the Walker strain fatigue law [19] of CMSX-4 at 927 °C gives a predicted crack initiation life of approximately 7600 cycles.

The critical crack length which marks the transition from crack initiation to crack propagation has been defined in commercial and military specifications as a 0.381mm surface crack or a 0.381mm radius corner crack [20, 21]. The area of such a corner crack is 0.114 mm^2. The equivalent area for a 30°/60°/90° right triangle has a hypotenuse of 0.513mm and this represents the equivalent critical crack length for a crack in the acute corner of the 30° angled hole configuration investigated here. As shown in Figure 14(c), 7600 cycles correspond approximately to a 0.5 mm crack. This shows that the mechanical hole drilling process into CMSX-4 thin wall samples that are subsequently coated with a diffusion coating has caused no significant debit to fatigue at 937°C in terms of fatigue crack growth to about 0.5 mm in size.

361

Conclusions

Tests and analyses of stress rupture and fatigue of thin wall CMSX-4 single crystals with small cooling holes have led to the following conclusions:

1. The effect of thin wall material degradation by environmental reaction or reaction with the coating material can be modeled using the concept of effective degradation thickness and effective stress.

2. The effective degradation thickness depends on stress and temperature through a power-law Arrhenius relationship.

3. The effective degradation thickness model allows the prediction of the stress rupture of thin walls by modifying rupture models ordinarily appropriate for solid bars.

4. Under cyclic in-plane compressive loading that mimics the service stresses in turbine vanes, fatigue cracks at cooling holes in thin walls are driven by local cyclic tensile stresses developed as a result of local plastic deformation.

5. For Pt aluminide coated CMSX-4 thin wall samples with cooling holes, the hole drilling process introduced no significant debit to the development of macroscopic fatigue cracks.

Acknowledgements

References

1. D. N. Duhl: "Directionally Solidified Superalloys," in *Superalloys II*, ed. C. T. Sims, N. S. Stoloff and W. C. Hagel, John Wiley, New York, pp. 189-214 (1987).

2. M. Doner and J. A. Heckler: "Identification of Mechanisms Responsible for Degradation in Thin-Wall Stress-Rupture Properties," in *Superalloys 1988 – Proceedings of the 6th International Symposium on Superalloys*, ed. S. Reichman, D.N. Duhl, G. Maurer, S. Antolovich and C. Lund, The Metallurgical Society, pp. 653-662 (1988).

3. V. Seetharaman and A. D. Cetel: "Thickness Debit in Creep Properties of PWA 1484," in *Superalloys 2004*, ed. K. A. Green, T. M. Pollock, H. Harada, T. E. Howson, R. C. Reed, J. J. Schirra and S. Walston, The Minerals, Metals & Materials Society, pp.207-214 (2004).

4. M. O. Lai and S. F. Koh: "Fatigue Performance of Holes with Different Finishing Processes," J. Mater. Proc. Tech., 44, pp.118-128 (1994).

5. Y. Pana, B. Bischoff-Beiermanna and T. Schulenberga: "Material Testing for Fatigue Design of Heavy-Duty Gas Turbine Blading with Film Cooling," Fatigue Design and Reliability, 23, pp. 155-162 (1999).

6. T. C. Totemeijer and J. E. King, "Isothermal Fatigue of an Aluminide-Coated Single Crystal Superalloy," Metall. Mater. Trans. A, 27A, pp.353-362 (1996).

7. R. C. Reed, *Superalloys: Fundamentals and Applications*, Cambridge University Press (2006).

8. N. Birks, G. H. Meier, and F. S. Pettit, Introduction to the High-Temperature Oxidation of Metals, Cambridge University Press, 2006.

9. B. Cassenti and A. Staroselsky: "The effect of thickness on the creep response of thin-wall single crystal components," Mater. Sci. Eng. A, vol. 508, pp. 183-189 (2009).

10. W. Li, Rolls-Royce internal document (2011).

11. M. Winning, G. Gottstein, and L. S. Shvindlerman, "Stress Induced Grain Boundary Motion", Acta. Mater., vol. 49, pp.211-219 (2001).

12. B. Hutchinson and B. Wynne, "Effects of Stress on Structure Transformations in Metals," Materials Science Forum, vol. 550, pp. 149-158 (2007).

13. L. M. Pan, B. A. Shollock and M. McLean: "Modeling of High Temperature Mechanical Behavior of a Single Crystal Superalloy," Proc. R. Soc. Lond. A, vol. 453, pp.1689-1715 (1997).

14. L. W. Candler and M. R. Winstone: "An Evaluation of Creep Behavior Models for Gas Turbine Alloys," in *High Temperature Materials for Power Engineering*, ed. E. Bachelet et al, Kluwer Academic Publishers, pp. 1077-1085 (1990).

15. D. W. MacLachlan, L. W. Wright, S. Gunturi, and D. M. Knowles: "Constitutive Modeling of Anisotropic Creep Deformation in Single Crystal Blade Alloys SRR99 and CMSX-4" Int. J. Plasticity, 17, pp.441-467 (2001).

16. R. E. Peterson: "Notch Sensitivity," in *Metal Fatigue*, McGraw-Hill, New York, pp.293-306 (1959).

17. D. Taylor: "Geometrical Effects in Fatigue: a Unifying Theoretical Model," Int. J. Fatigue, vol. 21, pp.413-420 (1999).

18. X. Yang, J. Wang and J. Liu, "High Temperature LCF Life Prediction of Notched DS Ni-Based Superalloy Using Critical Distance Concept," Int. J. Fatigue, vol. 33, pp.1470-1476 (2011).

19. K. Walker, "The Effect of Stress Ratio During Crack Propagation and Fatigue for 2024-T3 and 7075-T6 Aluminum," in *Effects of Environment and Complex Load History on Fatigue Life*, ASTM STP 462, pp.1-14 (1970).

20. Federal Aviation Administration Advisory Circular, No 33.70-1 (2009).

21. Department of Defense Handbook, "Engine Structural Integrity Program," MIL-Handbook-1783 (1997).